Investigation of image magnification properties of hyperlenses formed by a tapered array of metallic wires using a spatially dispersive finite-difference time-domain method in cylindrical coordinates

2012 J. Opt. 14 035102

(http://iopscience.iop.org/2040-8986/14/3/035102)

IOP Publishing Journal of Optics A: Pure and Applied Optics
J. Opt. **14** (2012) 035102 (9pp) doi:10.1088/2040-8978/14/3/035102

Investigation of image magnification properties of hyperlenses formed by a tapered array of metallic wires using a spatially dispersive finite-difference time-domain method in cylindrical coordinates

Yan Zhao

International School of Engineering, Faculty of Engineering, Chulalongkorn University, 254 Phayathai Road, Pathumwan, Bangkok 10330, Thailand

E-mail: yan.z@chula.ac.th

Received 11 November 2011, accepted for publication 6 January 2012
Published 2 February 2012
Online at stacks.iop.org/JOpt/14/035102

Abstract
In this paper, the spatially dispersive finite-difference time-domain (FDTD) method in cylindrical coordinates is applied to model the hyperlenses formed by a tapered array of metallic wires. The hyperlens device is modeled using the effective medium theory as a frequency and spatially dispersive dielectric. The gradual increase in spacing between wires along the radial direction of the physical structure is represented by the reduction of plasma frequency of the effective medium. Simulation results show that the image transfer and magnification capability of the hyperlens is insensitive to its transverse dimension. A seven-fold magnification of a subwavelength source distribution transferred to a distance of three wavelengths is demonstrated using a hyperlens with high plasma frequency at its front interface.

Keywords: cylindrical coordinates, finite-difference time-domain (FDTD), hyperlens, wire medium

(Some figures may appear in colour only in the online journal)

1. Introduction

A considerable amount of research effort has recently been spent on the development of subwavelength imaging devices. The concept of a 'perfect lens' was originally proposed by Pendry [1], using the so-called left-handed materials (LHMs) [2]. The principle of operation of such devices is based on the negative refraction of propagating waves and the amplification of evanescent field components. However, the resonant excitation of surface plasmons that causes evanescent wave amplification is sensitive to losses in LHM and hence limits the maximum thickness of the device [3].

An alternative way of subwavelength imaging has been suggested in the literature and termed as 'canalization' [4]. Its operation is based on the fact that for a certain type of device, the evanescent wave components can be transformed into propagating waves, and therefore the source field can be delivered to its back interface with little or no deterioration. In contrast to the case of LHM, such devices are less sensitive to losses. Typical examples of structures operating in the canalization regime include the wire medium

formed by an array of parallel conducting wires [5], and the layered structure consisting of materials with alternating positive and negative permittivity [6]. The thickness of both structures needs to be equal to an integer multiple of a half wavelength at the operating frequency (due to the Fabry–Pérot resonance), in order to avoid reflections between the source and the structure. It has been demonstrated numerically and experimentally that such a canalization regime indeed exists, and subwavelength details can be transferred to significant distances at frequencies up to the terahertz (THz) and infrared range [7, 8].

Recently, there has been a growing interest in the development of devices that are capable of simultaneously imaging and magnifying subwavelength field distributions in the visible frequency range [9–11]. In analogy to the perfect lens, such devices are termed as hyperlenses. Both the wire medium and the layered structure have been considered in constructing hyperlenses in the literature. In the visible frequency range, the hyperlens can be formed by either the layered structure with dielectric–plasmonic materials arranged uniaxially in Cartesian or cylindrical coordinates, or the plasmonic wire medium [12]. In microwave frequencies, the simultaneous enhancement and magnification of evanescent field patterns have been demonstrated experimentally with the help of double cylindrical polariton resonant structures by Alitalo *et al* [13] and numerically using a tapered array of metallic wires simulated using a commercial full-wave electromagnetic solver, FEKO [14].

Numerical modeling has always played an important role in the analysis and design of metamaterials. Owing to its simplicity and ability to handle inhomogeneous and anisotropic materials, the finite-difference time-domain (FDTD) method [15, 16] has become one of the most widely used numerical techniques. It has been applied to model the perfect lens formed by LHM [17], the wire medium (using the effective medium theory) [18], plasmonic structures [19], cloaking devices [20, 21], etc. However, all the above implementations of the FDTD method are performed in Cartesian coordinates and therefore staircase approximations need to be applied when modeling curved surfaces. In the modeling of hyperlenses which often possess cylindrical or spherical symmetry, the most suited approach is to apply the FDTD method in cylindrical or spherical coordinates. In this paper, we focus on the numerical modeling of hyperlens structures and propose a spatially dispersive FDTD method in cylindrical coordinates to model the hyperlens formed by a tapered array of metallic wires using the effective medium theory. Not only is the developed method more efficient compared with commercial electromagnetic solvers since the fine details of the hyperlens are not taken into account, but it offers flexibility in varying material parameters and dimensions of the structure such as its length, magnification ratio, etc.

2. FDTD modeling of hyperlenses formed by a tapered array of metallic wires

The conventional FDTD method deals with frequency-independent materials [15]. However, for the case of metamaterials which possess negative permittivity and/or permeability that can only be realized through material frequency dispersion, the dispersive FDTD method [16] needs to be applied. There also exist various dispersive FDTD methods using different approaches to deal with the frequency-dependent material parameters: the recursive convolution (RC) method, the auxiliary differential equation (ADE) method and the Z-transform method [16]. Due to its simplicity, the ADE method is applied to model hyperlens structures in this paper.

The ADE dispersive FDTD method is based on Faraday's and Ampère's laws

$$\nabla \times \mathbf{E} = -\frac{\partial \mathbf{B}}{\partial t}, \qquad \nabla \times \mathbf{H} = \frac{\partial \mathbf{D}}{\partial t}, \tag{1}$$

as well as the constitutive relations $\mathbf{D} = \varepsilon \mathbf{E}$ and $\mathbf{B} = \mu \mathbf{H}$. To simplify our analysis, in the current work we only consider the two-dimensional (2D) hyperlens which has cylindrical symmetry and only electric properties ($\mu = \mu_0$). The extension to the general three-dimensional (3D) case to model the spherical hyperlens is straightforward. Under the 2D assumption and due to the fact that the operation of a cylindrical hyperlens requires the electric field component to be aligned along its longitudinal direction, the expanded form of equations (1) in cylindrical coordinates for the 2D transverse electric (TE_z) case in the frequency domain is used:

$$\begin{aligned} \mathrm{j}\omega\mu_0 H_z &= \frac{1}{r}\frac{\partial E_r}{\partial \phi} - \frac{1}{r}\frac{\partial (rE_\phi)}{\partial r}, \\ \mathrm{j}\omega\varepsilon_r D_r = \frac{1}{r}\frac{\partial H_z}{\partial \phi}, &\qquad \mathrm{j}\omega\varepsilon_\phi D_\phi = -\frac{\partial H_z}{\partial r}, \end{aligned} \tag{2}$$

where

$$D_r = \varepsilon_r E_r, \qquad D_\phi = \varepsilon_\phi E_\phi. \tag{3}$$

In addition to Maxwell's equations, at the outer boundary of the computational domain, an absorbing boundary condition (ABC) needs to be applied in order to model an unbounded space. The original proposed perfectly matched layer (PML) by Berenger [22] has excellent performance but is only applicable to the Cartesian coordinates [23]. Hence in this work, we implement the complex coordinate stretching based PML through the change of variable [24]:

$$\bar{r} = r + \frac{1}{\mathrm{j}\omega\varepsilon_0}\int_0^r \sigma(s)\,\mathrm{d}s = r + \frac{\overline{\sigma}}{\mathrm{j}\omega\varepsilon_0}, \tag{4}$$

where $\sigma(s)$ is the conductivity term and

$$\overline{\sigma} = \int_0^r \sigma(s)\,\mathrm{d}s. \tag{5}$$

By splitting the H_z component [23], equations (2) read

$$\mathrm{j}\omega\mu_0\overline{H_{zr}} + \sigma^*\overline{H_{zr}} = -\frac{\partial \overline{E_\phi}}{\partial r}, \tag{6}$$

$$\mathrm{j}\omega r\mu_0 H_{z\phi} + \overline{\sigma^*} H_{z\phi} = \frac{\partial E_r}{\partial \phi}, \tag{7}$$

$$\mathrm{j}\omega r D_r + \frac{\overline{\sigma}}{\varepsilon_0} D_r = \frac{\partial H_z}{\partial \phi}, \tag{8}$$

$$\mathrm{j}\omega D_\phi + \frac{\sigma}{\varepsilon_0} D_\phi = -\frac{\partial H_z}{\partial r}, \tag{9}$$

$$\overline{H_{zr}} = \overline{r} H_{zr}, \tag{10}$$

$$\overline{E_\phi} = \overline{r} E_\phi, \tag{11}$$

where the chain rule $\partial/\partial r = (\partial/\partial\overline{r})(\partial\overline{r}/\partial r)$ is applied, and σ^* and $\overline{\sigma^*}$ are defined as

$$\sigma^* = \sigma\frac{\mu_0}{\varepsilon_0}, \qquad \overline{\sigma^*} = \overline{\sigma}\frac{\mu_0}{\varepsilon_0}. \tag{12}$$

Applying the inverse Fourier transform and using $\mathrm{j}\omega \to \partial/\partial t$, the above equations (6)–(11) can be written in the time domain as

$$\mu_0\frac{\partial \overline{H_{zr}}}{\partial t} + \sigma^*\overline{H_{zr}} = -\frac{\partial \overline{E_\phi}}{\partial r}, \tag{13}$$

$$\mu_0 r\frac{\partial H_{z\phi}}{\partial t} + \overline{\sigma^*} H_{z\phi} = \frac{\partial E_r}{\partial \phi}, \tag{14}$$

$$r\frac{\partial D_r}{\partial t} + \frac{\overline{\sigma}}{\varepsilon_0} D_r = \frac{\partial H_z}{\partial \phi}, \tag{15}$$

$$\frac{\partial D_\phi}{\partial t} + \frac{\sigma}{\varepsilon_0} D_\phi = -\frac{\partial H_z}{\partial r}, \tag{16}$$

$$r\frac{\partial H_{zr}}{\partial t} + \frac{\overline{\sigma^*}}{\mu_0} H_{zr} = \frac{\partial \overline{H_{zr}}}{\partial t}, \tag{17}$$

$$r\frac{\partial E_\phi}{\partial t} + \frac{\overline{\sigma}}{\varepsilon_0} E_\phi = \frac{\partial \overline{E_\phi}}{\partial t}. \tag{18}$$

The FDTD simulation domain is represented by an equally spaced 2D grid with periods Δr and $\Delta\phi$ along the r- and ϕ-directions, respectively. For the discretization of equations (13)–(18), we use the central finite-difference operators in space (δ_r, δ_ϕ), in time (δ_t), and the central average operator in time (μ_t):

$$\frac{\partial}{\partial r} \to \frac{\delta_r}{\Delta r}, \qquad \frac{\partial}{\partial \phi} \to \frac{\delta_\phi}{\Delta\phi},$$
$$\frac{\partial}{\partial t} \to \frac{\delta_t}{\Delta t}, \qquad 1 \to \mu_t,$$

where the operators δ_r, δ_ϕ, δ_t, and μ_t are defined as [25]:

$$\begin{aligned}
\delta_r \mathbf{F}|^n_{m_r,m_\phi} &\equiv \mathbf{F}|^n_{m_r+\frac{1}{2},m_\phi} - \mathbf{F}|^n_{m_r-\frac{1}{2},m_\phi},\\
\delta_\phi \mathbf{F}|^n_{m_r,m_\phi} &\equiv \mathbf{F}|^n_{m_r,m_\phi+\frac{1}{2}} - \mathbf{F}|^n_{m_r,m_\phi-\frac{1}{2}},\\
\delta_t \mathbf{F}|^n_{m_r,m_\phi} &\equiv \mathbf{F}|^{n+\frac{1}{2}}_{m_r,m_\phi} - \mathbf{F}|^{n-\frac{1}{2}}_{m_r,m_\phi},\\
\mu_t \mathbf{F}|^n_{m_r,m_\phi} &\equiv \frac{\mathbf{F}|^{n+\frac{1}{2}}_{m_r,m_\phi} + \mathbf{F}|^{n-\frac{1}{2}}_{m_r,m_\phi}}{2},
\end{aligned} \tag{19}$$

where $\mathbf{F}$ represents field components and m_r, m_ϕ are the indices corresponding to a certain discretization point in the FDTD domain. The discretized equations (13)–(18) read

$$\mu_0\frac{\delta_t}{\Delta t}\overline{H_{zr}} + \sigma^*\mu_t\overline{H_{zr}} = -\frac{\delta_r}{\Delta r}\overline{E_\phi}, \tag{20}$$

$$\mu_0 r\frac{\delta_t}{\Delta t} H_{z\phi} + \overline{\sigma^*}\mu_t H_{z\phi} = \frac{\delta_\phi}{\Delta\phi} E_r, \tag{21}$$

$$r\frac{\delta_t}{\Delta t} D_r + \frac{\overline{\sigma}}{\varepsilon_0}\mu_t D_r = \frac{\delta_\phi}{\Delta\phi} H_z, \tag{22}$$

$$\frac{\delta_t}{\Delta t} D_\phi + \frac{\sigma}{\varepsilon_0}\mu_t D_\phi = -\frac{\delta_r}{\Delta r} H_z, \tag{23}$$

$$r\frac{\delta_t}{\Delta t} H_{zr} + \frac{\overline{\sigma^*}}{\mu_0}\mu_t H_{zr} = \frac{\delta_r}{\Delta t}\overline{H_{zr}}, \tag{24}$$

$$r\frac{\delta_t}{\Delta t} E_\phi + \frac{\overline{\sigma}}{\varepsilon_0}\mu_t E_\phi = \frac{\delta_t}{\Delta t}\overline{E_\phi}. \tag{25}$$

Applying the operators (19) and rearranging terms, the following FDTD updating equations can be obtained:

$$\begin{aligned}
\overline{E_\phi}|^{n+\frac{1}{2}}_{m_r,m_\phi} = \overline{E_\phi}|^{n-\frac{1}{2}}_{m_r,m_\phi} &+ \left(r + \frac{\overline{\sigma}\Delta t}{2\varepsilon_0}\right) E_\phi|^{n+\frac{1}{2}}_{m_r,m_\phi}\\
&- \left(r - \frac{\overline{\sigma}\Delta t}{2\varepsilon_0}\right) E_\phi|^{n-\frac{1}{2}}_{m_r,m_\phi},
\end{aligned} \tag{26}$$

$$\begin{aligned}
\overline{H_{zr}}|^{n+\frac{1}{2}}_{m_r,m_\phi} = &\left(\frac{2\mu_0 - \sigma^*\Delta t}{2\mu_0 + \sigma^*\Delta t}\right)\overline{H_{zr}}|^{n-\frac{1}{2}}_{m_r,m_\phi}\\
&- \frac{\overline{E_\phi}|^n_{m_r+\frac{1}{2},m_\phi} - \overline{E_\phi}|^n_{m_r-\frac{1}{2},m_\phi}}{\Delta r(2\mu_0 + \sigma^*\Delta t)/(2\Delta t)},
\end{aligned} \tag{27}$$

$$\begin{aligned}
H_{zr}|^{n+\frac{1}{2}}_{m_r,m_\phi} = &\left(\frac{2\mu_0 r - \overline{\sigma^*}\Delta t}{2\mu_0 r + \overline{\sigma^*}\Delta t}\right) H_{zr}|^{n-\frac{1}{2}}_{m_r,m_\phi}\\
&+ \frac{\overline{H_{zr}}|^{n+\frac{1}{2}}_{m_r,m_\phi} - \overline{H_{zr}}|^{n-\frac{1}{2}}_{m_r,m_\phi}}{\Delta t(2\mu_0 r + \overline{\sigma^*}\Delta t)/(2\mu_0\Delta t)},
\end{aligned} \tag{28}$$

$$\begin{aligned}
H_{z\phi}|^{n+\frac{1}{2}}_{m_r,m_\phi} = &\left(\frac{2\mu_0 r - \overline{\sigma^*}\Delta t}{2\mu_0 r + \overline{\sigma^*}\Delta t}\right) H_{z\phi}|^{n-\frac{1}{2}}_{m_r,m_\phi}\\
&+ \frac{E_r|^n_{m_r,m_\phi+\frac{1}{2}} - E_r|^n_{m_r,m_\phi-\frac{1}{2}}}{\Delta\phi(2\mu_0 r + \overline{\sigma^*}\Delta t)/(2\Delta t)},
\end{aligned} \tag{29}$$

$$H_z|^{n+\frac{1}{2}}_{m_r,m_\phi} = H_{zr}|^{n+\frac{1}{2}}_{m_r,m_\phi} + H_{z\phi}|^{n+\frac{1}{2}}_{m_r,m_\phi}, \tag{30}$$

$$\begin{aligned}
D_r|^{n+\frac{1}{2}}_{m_r,m_\phi} = &\left(\frac{2\varepsilon_0 r - \overline{\sigma}\Delta t}{2\varepsilon_0 r + \overline{\sigma}\Delta t}\right) D_r|^{n-\frac{1}{2}}_{m_r,m_\phi}\\
&+ \frac{H_z|^n_{m_r,m_\phi+\frac{1}{2}} - H_z|^n_{m_r,m_\phi-\frac{1}{2}}}{\Delta\phi(2\varepsilon_0 r + \overline{\sigma}\Delta t)/(2\varepsilon_0\Delta t)},
\end{aligned} \tag{31}$$

$$\begin{aligned}
D_\phi|^{n+\frac{1}{2}}_{m_r,m_\phi} = &\left(\frac{2\varepsilon_0 - \sigma\Delta t}{2\varepsilon_0 + \sigma\Delta t}\right) D_\phi|^{n-\frac{1}{2}}_{m_r,m_\phi}\\
&- \frac{H_z|^n_{m_r+\frac{1}{2},m_\phi} - H_z|^n_{m_r-\frac{1}{2},m_\phi}}{\Delta r(2\varepsilon_0 + \sigma\Delta t)/(2\varepsilon_0\Delta t)}.
\end{aligned} \tag{32}$$

In addition to the above updating equations, the dielectric properties of hyperlens structures need to be taken into account in FDTD simulations. These additional updating equations can be derived through the discretization of equations (3), which is introduced as follows.

The wire medium has been known for a long time as an artificial dielectric with plasma-like frequency-dependent permittivity [26, 27], but only recently it has been shown that this dielectric is non-local and possesses strong spatial dispersion even at very low frequencies [28]. Following [28], the wire medium can be described as a uniaxial dielectric (if the lattice period is much smaller than the wavelength) with both frequency and spatially dependent effective permittivity:

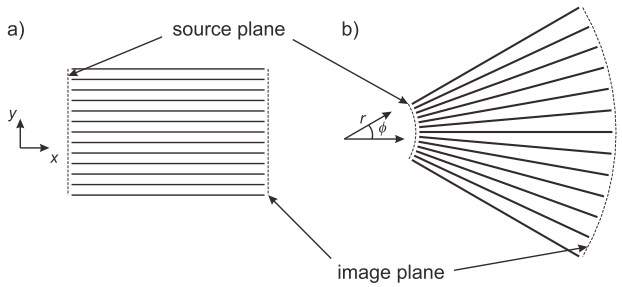

Figure 1. (a) The 2D view of a parallel wire medium as a transmission device. (b) The 2D view of a hyperlens formed by a tapered array of wires which can be conveniently represented in cylindrical coordinates.

$$\bar{\bar{\varepsilon}} = \varepsilon(k, q_x)\mathbf{xx} + \mathbf{yy} + \mathbf{zz},$$
$$\varepsilon(k, q_x) = \varepsilon_0\left(1 - \frac{k_\mathrm{p}^2}{k^2 - q_x^2}\right), \tag{33}$$

where $k_\mathrm{p} = \omega_\mathrm{p}/c$ is the wavenumber corresponding to the plasma frequency ω_p, $k = \omega/c$ is the wavenumber of free space, c is the speed of light, and q_x is the component of the wavevector along the wires. The dependence of permittivity equation (33) on q_x represents the spatial dispersion effect which is not taken into account in the conventional local uniaxial model of the wire medium [26, 27]. The k_p depends on the lattice periods (a, b) and the radius of wires (r) [28]:

$$k_\mathrm{p}^2 = \frac{2\pi/(ab)}{\log[\sqrt{ab}/(2\pi r)] + F(a/b)}, \tag{34}$$

where

$$F(\xi) = -\frac{1}{2}\log\xi + \sum_{n=1}^{+\infty}\left(\frac{\coth(\pi n\xi) - 1}{n}\right) + \frac{\pi}{6}\xi. \tag{35}$$

For the commonly used case of square grid $(a = b)$, $F(1) = 0.5275$.

The material properties of the wire medium specified in (33) are in Cartesian coordinates, and the parallel wires are aligned along the x-direction. For the construction of a hyperlens using an array of wires, the spacing of wires can be gradually increased from the front to the back interface of the device, as shown in figure 1(b). Thus the hyperlens can be represented in cylindrical coordinates for the 2D case or spherical/cylindrical coordinates for the 3D case, by assuming the wires are aligned along the radial direction. In the 2D TE_z case, the permittivity of the hyperlens is given by

$$\varepsilon_r(k, q_r) = \varepsilon_0\left[1 - \frac{k_\mathrm{p}^2(r)}{k^2 - q_r^2}\right], \qquad \varepsilon_\phi = \varepsilon_0. \tag{36}$$

In order to correctly model the wire medium by taking into account the spatial dispersion effect, a spatially dispersive FDTD method in Cartesian coordinates has been developed in [18]. For the modeling of a hyperlens with its permittivity specified in cylindrical coordinates using the conventional FDTD method, it is necessary to perform a coordinates transformation and convert the permittivity equations (36) to Cartesian coordinates in simulations, as has been done for the modeling of cylindrical cloaking devices in Cartesian FDTD simulations [20]. However, the angles involved in the transformation matrix need to be calculated numerically and staircase approximations are required to represent curved surfaces in a Cartesian grid. These approximations introduce numerical errors which reduce the simulation accuracy. Alternatively, the permittivity of the structure specified in cylindrical coordinates can be directly taken into account in the FDTD method in cylindrical coordinates.

Since the permittivity of the tapered array of wires along the ϕ-direction is equal to the free space one, the updating equation for the E_ϕ component can be directly expressed as

$$E_\phi|_{m_r,m_\phi}^{n+\frac{1}{2}} = \frac{1}{\varepsilon_0}D_\phi|_{m_r,m_\phi}^{n+\frac{1}{2}}. \tag{37}$$

For the r-component of electric field, since $D_r(\omega, q_r)$ is related to $E_r(\omega, q_r)$ in the spectral (frequency-wavevector) domain as

$$D_r(\omega) = \varepsilon(\omega, q_r)E_r(\omega), \tag{38}$$

one can write that

$$(k^2 - q_r^2)D_r + (q_r^2 - k^2 + k_\mathrm{p}^2)\varepsilon_0 E_r = 0. \tag{39}$$

Using inverse Fourier transformation and the following rules:

$$k^2 \to -\frac{1}{c^2}\frac{\partial^2}{\partial t^2}, \qquad q_r^2 \to -\frac{\partial^2}{\partial r^2}, \tag{40}$$

the constitutive relation in the time–space domain can be written as

$$\left(\frac{\partial^2}{\partial r^2} - \frac{1}{c^2}\frac{\partial^2}{\partial t^2}\right)D_r + \left(\frac{1}{c^2}\frac{\partial^2}{\partial t^2} - \frac{\partial^2}{\partial r^2} + k_\mathrm{p}^2\right)\varepsilon_0 E_r = 0. \tag{41}$$

The above equation can be discretized using the following operators [25]:

$$\begin{aligned}
\delta_t^2\mathbf{F}|_{m_r,m_\phi}^n &\equiv \mathbf{F}|_{m_r,m_\phi}^{n+1} - 2\mathbf{F}|_{m_r,m_\phi}^n + \mathbf{F}|_{m_r,m_\phi}^{n-1},\\
\delta_r^2\mathbf{F}|_{m_r,m_\phi}^n &\equiv \mathbf{F}|_{m_r+1,m_\phi}^n - 2\mathbf{F}|_{m_r,m_\phi}^n + \mathbf{F}|_{m_r-1,m_\phi}^n,\\
\mu_t^2\mathbf{F}|_{m_r,m_\phi}^n &\equiv \frac{F|_{m_r,m_\phi}^{n+1} + 2\mathbf{F}|_{m_r,m_\phi}^n + \mathbf{F}|_{m_r,m_\phi}^{n-1}}{4}.
\end{aligned} \tag{42}$$

Thus the updating equation for the E_r component can be derived as

$$\begin{aligned}
E_r|_{m_r,m_\phi}^{n+1} = \Bigg\{ &-\frac{1}{c^2(\Delta t)^2}D_r|_{m_r,m_\phi}^{n+1} + \frac{1}{(\Delta r)^2}D_r|_{m_r+1,m_\phi}^n\\
&+ \frac{1}{(\Delta r)^2}D_r|_{m_r-1,m_\phi}^n - \frac{1}{c^2(\Delta t)^2}D_r|_{m_r,m_\phi}^{n-1}\\
&+ \left[\frac{2}{c^2(\Delta t)^2} - \frac{2}{(\Delta r)^2}\right]D_r|_{m_r,m_\phi}^n - \frac{\varepsilon_0}{(\Delta r)^2}E_r|_{m_r+1,m_\phi}^n\\
&- \left[\frac{2\varepsilon_0}{c^2(\Delta t)^2} - \frac{2\varepsilon_0}{(\Delta r)^2} - \frac{\varepsilon_0 k_\mathrm{p}^2}{2}\right]E_r|_{m_r,m_\phi}^n\\
&- \frac{\varepsilon_0}{(\Delta r)^2}E_r|_{m_r-1,m_\phi}^n + \left[\frac{\varepsilon_0}{c^2(\Delta t)^2}\right.\\
&\left. + \frac{\varepsilon_0 k_\mathrm{p}^2}{4}\right]E_r|_{m_r,m_\phi}^{n-1}\Bigg\} \Bigg/ \left[\frac{\varepsilon_0}{c^2(\Delta t)^2} + \frac{\varepsilon_0 k_\mathrm{p}^2}{4}\right].
\end{aligned} \tag{43}$$

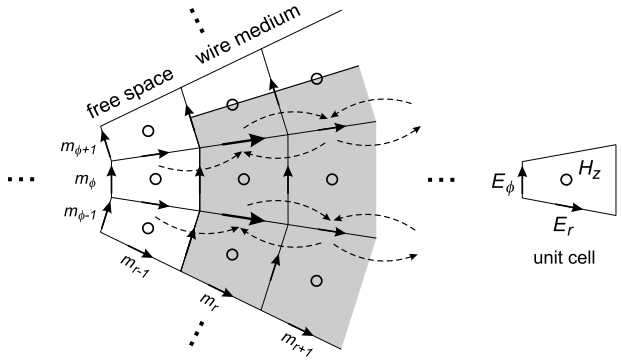

Figure 2. A partial grid layout in cylindrical FDTD domain for the modeling of a hyperlens formed by a tapered array of wires. The dashed arrows indicate the dependency between adjacent field components.

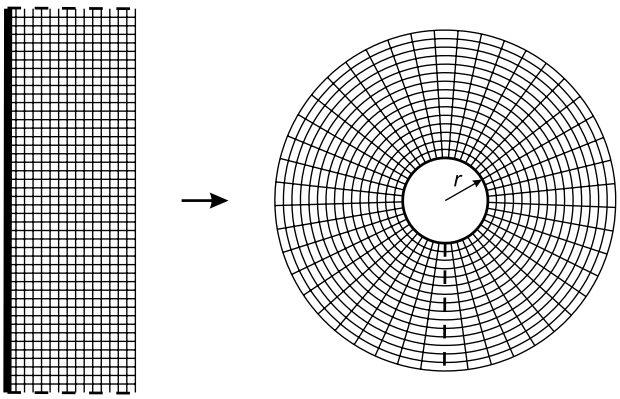

Figure 3. Mapping of a 2D array to the FDTD grid in cylindrical coordinates. The thick solid/dashed lines indicate the same array of elements.

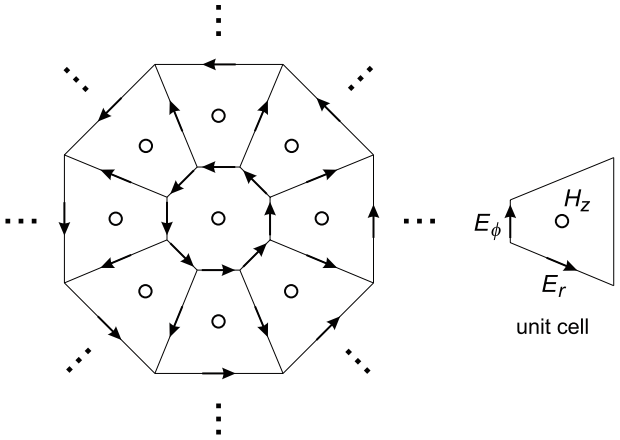

Figure 4. Layout of the FDTD grid in cylindrical coordinates in the vicinity of the origin, where the H_z component is located and treated separately.

Note from equation (34) that k_p depends on the spacing between wires. Hence in the simulation of the hyperlens structure in which the spacing gradually increases from the front interface of the device to its back one, k_p needs to be reduced accordingly.

In equation (43), the central finite-difference approximations in time (for the frequency dispersion) for both D_r and E_r are used at position m_r, and the central finite-difference approximations in space (for the spatial dispersion) are used at the time step n in order to update E_r^{n+1}. Therefore the storage of D_r and E_r at two previous time steps is required. At the free space-tapered array interface along the r-direction, the updating equation (43) involves D_r and E_r in both free space and the tapered array, as indicated by the large arrows in figure 2. Outside the region of the tapered array, the updating equation (43) reduces to the equation relating D_r and E_r in free space, which can be realized by letting the plasma frequency equal zero ($k_p = 0$). Along the ϕ-direction, the transverse dimension of the hyperlens, w, can be equal to either a complete circle of 2π rad, or a finite angular length. For the case of $w = 2\pi$, no material interfaces exist thus no special treatment is necessary; while for the modeling of a hyperlens with finite transverse dimension, the boundary of the tapered array needs to be aligned with the H_z component to avoid the averaging of material parameters of the free space and the tapered array at their interface [17], as illustrated in figure 2. Equations (26)–(32), (37), and (43) form a complete set of updating equations for the modeling of the hyperlens formed by a tapered array of wires.

For the computer programming of the conventional FDTD method in Cartesian coordinates, 2D arrays are often used to store field values conveniently. However, in cylindrical coordinates, a mapping of 2D arrays to the FDTD grid needs to be performed. Figure 3 shows the mapping of a 15 × 45-element array to a cylindrical FDTD grid, where the first column of the array is mapped to the inner boundary of the grid, as indicated by the thick solid lines. The top and bottom rows of the 2D array merge together to form the same array of radial elements, as shown by the thick dashed lines. Due to the merging, the original boundaries where the arrays are located disappear, and the FDTD updating equations need to be modified accordingly. Note that such a way of mapping is different from the conventional implementation of the FDTD method in cylindrical coordinates which directly assumes the radius of the grid to be equal to zero. This approach allows one to model a perfect electric conductor (PEC) centered at the origin with reduced computer memory since no fields can enter the area enclosed by PEC thus no FDTD grids need to be assigned in that region. However, for the modeling of free space at the origin, it is necessary to set $r = 0$. Then the issue of numerical singularity at the origin arises. Figure 4 shows an example of a detailed FDTD grid layout in cylindrical coordinates in the vicinity of the origin for the case of eight elements along the ϕ-direction (for illustration purposes). In general, either the E_z or H_z component can be assumed to be located at the origin. In our 2D case, the non-zero component is H_z, it is then aligned with the origin of the coordinates and treated separately from FDTD updating equations to avoid the singularity issue.

Methods for dealing with the numerical singularity at the origin have been proposed in [29–31]. Following the same approach as in [30, 31] by evaluating the integral form of Faraday's law, the H_z component at the origin can be

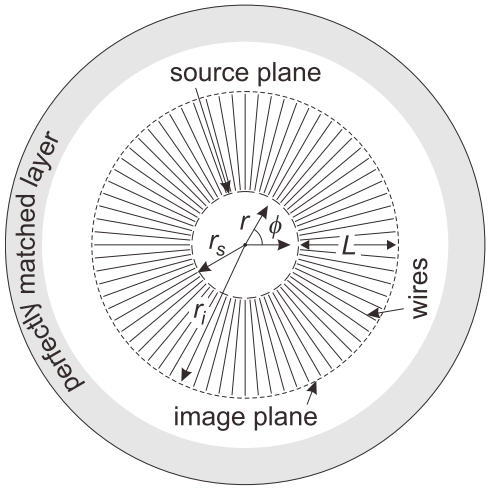

Figure 5. The 2D FDTD simulation domain in cylindrical coordinates for the modeling of a hyperlens formed by a tapered array of wires.

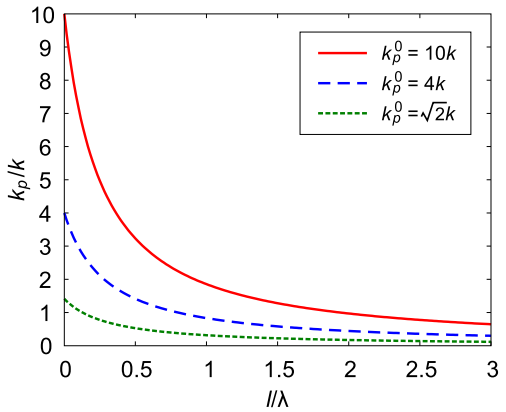

Figure 6. Normalized value of k_p versus the location within the hyperlens (with reference to the inner interface), where k_p^0 is the value of k_p at the inner interface.

calculated as

$$H_z\big|_{0,m_\phi}^{n+\frac{1}{2}} = H_z\big|_{0,m_\phi}^{n-\frac{1}{2}} - \frac{4\Delta t}{\mu_0 N_\phi \Delta r}\sum_{k=1}^{N_\phi} E_\phi\Big|_{1,k}^{n}, \tag{44}$$

where N_ϕ is the number of elements along the ϕ-direction.

At the outer boundary of the FDTD domain, in order to model an unbounded space, the above introduced complex coordinate stretching based PML can be applied by gradually increasing the conductivity term from zero to its maximum value, $\sigma_{\max}$, which is defined as

$$\sigma_{\max} = -\frac{(m+1)\ln[R(0)]}{2N_{\text{PML}}\Delta r\sqrt{\mu_0/\varepsilon_0}}, \tag{45}$$

where $R(0)$ is the reflection coefficient at normal incidence between the free space and the PML layer, and N_{PML} is the number of cells in the PML layer. The value of the conductivity term in each PML layer can be calculated as

$$\sigma(n) = \sigma_{\max}\left(\frac{n}{N_{\text{PML}}}\right)^m, \tag{46}$$

where the layer index, n, is an integer and $1 \le n \le N_{\text{PML}}$. Then the integral factor can be numerically calculated as

$$\overline{\sigma} = \int_0^r \sigma(s)\,\mathrm{d}s = \frac{\sigma_{\max} n\Delta r}{m+1}\left(\frac{n}{N_{\text{PML}}}\right)^m. \tag{47}$$

In the above equations, m defines the profile of the location-dependent conductivity term within the PML layer and satisfactory results can be obtained by letting $m = 2$. The outermost layer of the PML is defined as the PEC condition by specifying zero values for the tangential electric field component, E_ϕ.

For stable FDTD simulations, the time step Δt needs to be bounded by the following condition [16]:

$$c\Delta t \le \frac{1}{\sqrt{1/\Delta r^2 + 1/(\Delta r\Delta\phi)^2}}. \tag{48}$$

It is worth mentioning that since the FDTD spatial resolution decreases toward the boundary of the cylindrical domain due to the expansion of the unit cell along the radial direction, for the simulation of large domains, it is necessary to ensure that the largest mesh size is small enough (e.g. $r\Delta\phi < \lambda/20$) to guarantee sufficient numerical accuracy.

The developed cylindrical FDTD method has been implemented to investigate the image transfer and magnification capability of the hyperlens. The simulation results are presented in section 3.

3. Numerical results and discussions

The 2D FDTD simulation domain is shown in figure 5, where the outer boundary of the domain is terminated by a 20-layer complex coordinates stretching based PML. The FDTD cell size along the r-direction is $\Delta r = \lambda/60$ where λ is the wavelength at the operating frequency of $f = 1.0$ GHz. The number of FDTD cells along the ϕ-direction is 800 in all simulations. Three magnetic line sources (located at equal distances to the origin) are excited at a distance of $\lambda/10$ to the front interface of the hyperlens. The distance between adjacent sources is $\lambda/20$ and the central source is excited out of phase with respect to the neighboring ones. The proposed three-source configuration creates a distribution with two strong maxima at the front interface of the hyperlens and the distance between the maxima is about $\lambda/5$.

In order to investigate the imaging and magnification properties of the hyperlens, various lengths, transverse (angular) dimensions of the device, and k_p are considered in simulations. The value of k_p can be calculated from equation (34) by choosing appropriate values of a, b, and r. Figure 6 shows the variation of normalized k_p versus the location l within the hyperlens (with reference to the inner interface) for three different cases: $k_p^0 = 10k$ ($a_0 = b_0 = 11.3$ mm), $k_p^0 = 4k$ ($a_0 = b_0 = 22.3$ mm), and $k_p^0 = \sqrt{2}k$ ($a_0 = b_0 = 52.1$ mm), where k_p^0 is the value of k_p at the inner interface, a_0 and b_0 are the lattice periods at the inner interface, and $r = 1$ mm. It can be seen that for all

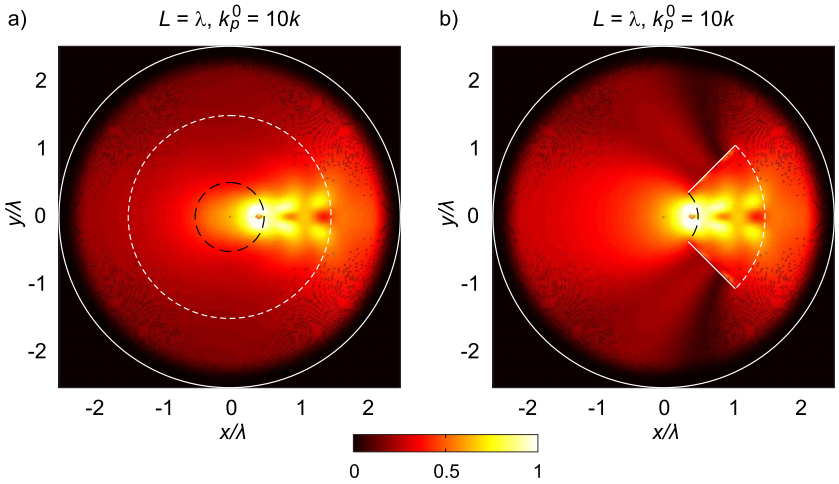

Figure 7. Normalized magnetic field distributions calculated from cylindrical FDTD simulations for two hyperlens structures with angular widths of (a) $w = 2\pi$ and (b) $w = \pi/4$.

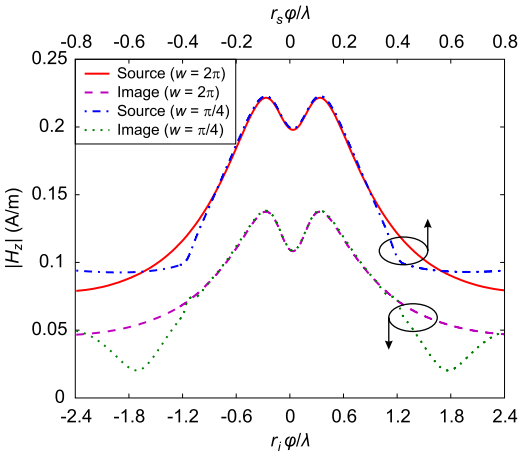

Figure 8. Comparison of magnetic field distributions at the source and image planes of two hyperlens structures with angular widths of $w = 2\pi$ and $\pi/4$. In both cases, $k_\mathrm{p}^0 = 10k$.

cases, as the spacing between wires increases, the value of k_p decreases accordingly, and becomes less than k beyond a certain location. However, the operation of the wire medium as a transmission device requires $k_\mathrm{p} > k$ [18]. This means that there may exist a maximum length for the proper operation of the device. This effect is demonstrated through the following simulation results.

It has been shown in [18] that due to the canalization principle which only allows waves to travel along the direction of wires, the subwavelength imaging property of the wire medium device is insensitive to its transverse dimension. It is also of practical importance to investigate whether the magnification of subwavelength distributions using a hyperlens formed by a tapered array of wires is affected by its angular dimension, w. Figure 7 shows the comparison of magnetic field distributions using two hyperlens structures with $w = 2\pi$ and $w = \pi/4$, respectively. For both devices: $k_\mathrm{p}^0 = 10k$, the length is $L = \lambda$, and the locations of the inner and outer interfaces are $r_\mathrm{s} = \lambda/2$ and $r_\mathrm{i} = 3\lambda/2$, respectively (see figure 5). The magnetic field distributions at the source and image planes of both devices are plotted in figure 8. The nearly identical field distributions within the area of the device between the cases of $w = 2\pi$ and $\pi/4$ demonstrate that the image magnification property of the hyperlens is insensitive to its transverse (angular) dimension. In addition, since the angular width increases from the inner interface to the outer one by three times, a three-fold magnification of subwavelength source distribution is observed, as shown by the two clearly resolved maxima at the image plane in figure 8. In the rest of the simulations, the angular width is always kept as $w = \pi/4$.

In order to investigate the effect of varying k_p^0 on the image magnification capability of the hyperlens, different values of k_p^0 are chosen in simulations. Moreover, when the value of k_p^0 is large, the device can be approximated to have infinite permittivity along the radial direction, i.e. $E_r = 0$. Hence simulations are performed for two hyperlens devices with $\varepsilon_r = \infty$ and $k_\mathrm{p}^0 = \sqrt{2}k$, respectively. The rest of the parameters remain unchanged. The magnetic field distributions for these structures are shown in figure 9, and the comparison of magnetic field distributions in the source and image planes of both devices is shown in figure 10. It can be seen that figures 9(a) and 7(b) have very similar distributions but figure 9(b) is considerably different. This is due to the small value of k_p^0 at the front interface, thus the value of k_p decreases to be less than k beyond a distance of 0.12λ from the source plane. Similar to the case of subwavelength imaging using the wire medium, the low value of k_p leads to the low imaging resolution of the device [18]. As a consequence, the two maxima at the image plane become much less distinguishable, as shown in figure 10.

If the length of the hyperlens is extended, it is expected that the maxima will be difficult to resolve with the device. Figure 11 shows magnetic field distributions for two 3λ-long hyperlens structures with $k_\mathrm{p}^0 = \sqrt{2}k$ and $k_\mathrm{p}^0 = 10k$, respectively. It can be seen that the distributions are dramatically different and the hyperlens with $k_\mathrm{p}^0 =$

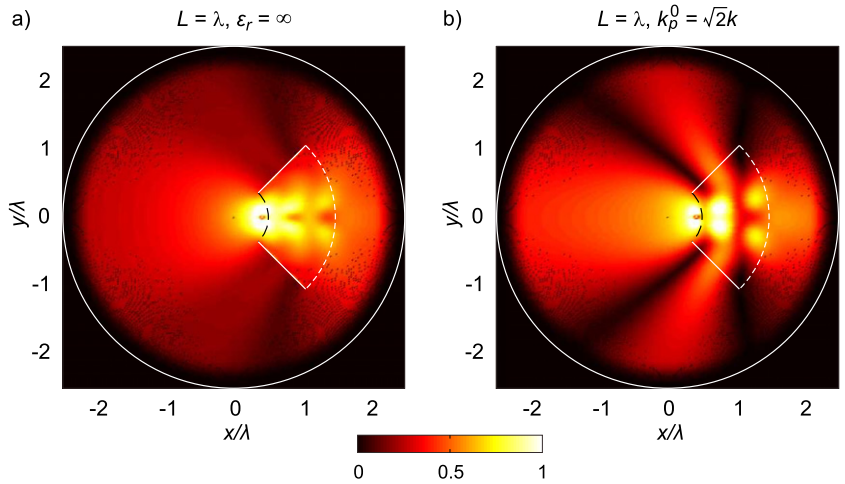

Figure 9. Normalized magnetic field distributions for two hyperlens structures with (a) $\varepsilon_r = \infty$ and (b) $k_{\rm p}^0 = \sqrt{2}k$. In both cases, $L = \lambda$.

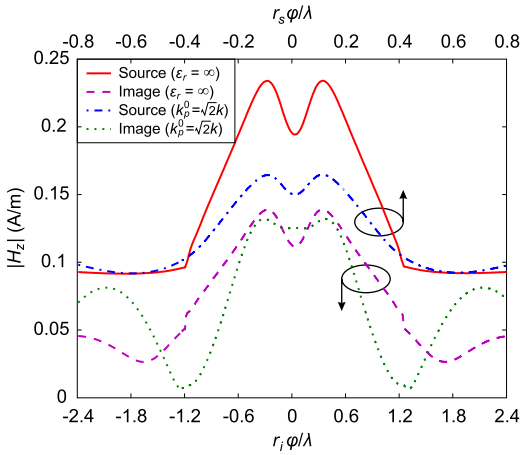

Figure 10. Comparison of magnetic field distributions in the source and image planes of two hyperlens structures with $\varepsilon_r = \infty$ and $k_{\rm p}^0 = \sqrt{2}k$. In both cases, $L = \lambda$.

$10k$ provides a seven-fold image magnification of the subwavelength source distribution, as shown in figure 12. The spacing between these maxima is 1.4λ thus they can be detected in far-field by conventional scanning devices. On the other hand, the hyperlens with $k_{\rm p}^0 = \sqrt{2}k$ introduces strong reflections which distort the distributions in both the source and image planes, resulting in two hardly distinguishable maxima. If the length of the device is further extended, the maxima may merge together and the subwavelength details of the source distribution may not be resolved at the image plane. This comparison clearly shows that for a hyperlens formed by a tapered array of metallic wires with a certain value of $k_{\rm p}^0$, there exists a maximum length below which the device can only be used for image transfer and magnification.

4. Conclusion

In conclusion, a spatially dispersive FDTD method in cylindrical coordinates is developed to model the hyperlens formed by a tapered array of metallic wires. The center of the device is aligned with the origin of the coordinates and the wires are along the radial directions. The hyperlens structure is modeled as a frequency and spatially dispersive dielectric using the effective medium theory, and the increase of the spacing between wires is represented by the gradual reduction

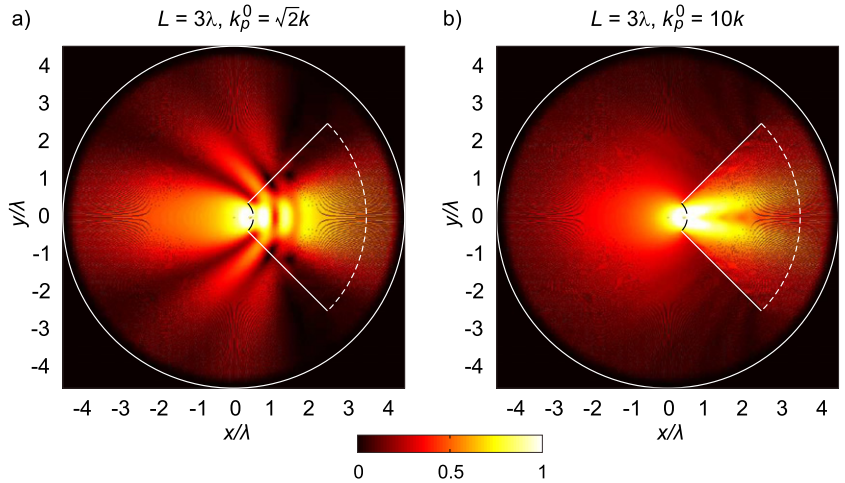

Figure 11. Normalized magnetic field distributions for two hyperlens structures with (a) $k_{\rm p}^0 = \sqrt{2}k$ and (b) $k_{\rm p}^0 = 10k$. In both cases, $L = 3\lambda$.

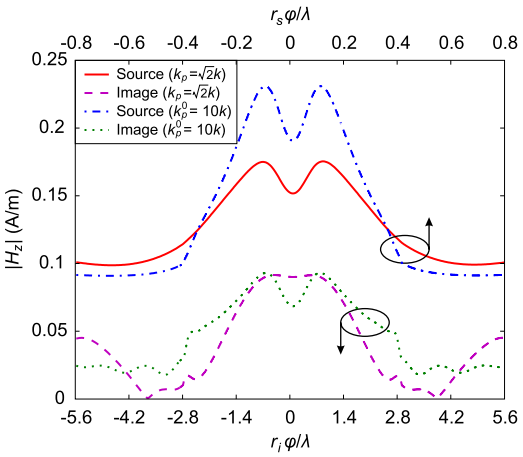

Figure 12. Comparison of magnetic field distributions in the source and image planes of two hyperlens structures with $k_\mathrm{p}^0 = \sqrt{2}k$ and $10k$. In both cases, $L = 3\lambda$.

of plasma frequency in FDTD simulations. Numerical results show that the image transfer and magnification capability of such hyperlens structures is insensitive to their transverse (angular) dimensions. A seven-fold magnification of a source distribution with $\lambda/5$ resolution to a distance of 3λ is demonstrated. However, for the hyperlens device considered in this paper, there exists a maximum length for the effective transfer and magnification of subwavelength source distributions to the far-field. Finally we would like to mention that using the method proposed in this paper, image demagnification properties of hyperlens devices formed by tapered arrays of wires can be analyzed conveniently.

References

[1] Pendry J 2000 Negative refraction index makes a perfect lens *Phys. Rev. Lett.* **85** 3966–9

[2] Veselago V G 1968 The electrodynamics of substances with simultaneously negative values of ε and μ *Sov. Phys.—Usp.* **10** 509–14

[3] Podolskiy V A and Narimanov E E 2005 Near-sighted superlens *Opt. Lett.* **30** 75–7

[4] Belov P A, Simovski C R and Ikonen P 2005 Canalization of subwavelength images by electromagnetic crystals *Phys. Rev.* B **71** 193105

[5] Belov P A, Hao Y and Sudhakaran S 2006 Subwavelength microwave imaging using an array of parallel conducting wires as a lens *Phys. Rev.* B **73** 033108

[6] Belov P A and Hao Y 2006 Subwavelength imaging at optical frequencies using a transmission device formed by a periodic layered metal–dielectric structure operating in the canalization regime *Phys. Rev.* B **73** 113110

[7] Shvets G, Trendafilov S, Pendry J B and Sarychev A 2007 Guiding, focusing, and sensing on the subwavelength scale using metallic wire arrays *Phys. Rev. Lett.* **99** 053903

[8] Belov P A, Simovski C R, Ikonen P, Silveirinha M G and Hao Y 2007 Image transmission with the subwavelength resolution in microwave, terahertz, and optical frequency bands *J. Commun. Technol. Electron.* **52** 1009

[9] Jacob Z, Alekseyev L V and Narimanov E 2006 Optical hyperlens: far-field imaging beyond the diffraction limit *Opt. Express* **14** 8247

[10] Liu Z, Lee H, Xiong Y, Sun C and Zhang X 2007 Far-field optical hyperlens magnifying sub-diffraction-limited objects *Science* **315** 1686

[11] Smolyaninov I I, Hung Y-J and Davis C C 2007 Magnifying superlens in the visible frequency range *Science* **315** 1699

[12] Kawata1 S, Ono A and Verma1 P 2008 Subwavelength colour imaging with a metallic nanolens *Nature Photon.* **2** 438–42

[13] Alitalo P, Maslovski S and Tretyakov S 2006 Near-field enhancement and imaging in double cylindrical polariton-resonant structures: enlarging superlens *Phys. Lett.* A **357** 397

[14] Ikonen P, Simovski C, Tretyakov S, Belov P and Hao Y 2007 Magnification of subwavelength field distributions at microwave frequencies using a wire medium slab operating in the canalization regime *Appl. Phys. Lett.* **91** 104102

[15] Yee K S 1966 Numerical solution of initial boundary value problems involving Maxwell's equations in isotropic media *IEEE Trans. Antennas Propag.* **14** 302–7

[16] Taflove A 2000 *Computational Electrodynamics: The Finite-Difference Time-Domain Method* 2nd edn (Norwood, MA: Artech House Publishers)

[17] Zhao Y, Belov P A and Hao Y 2007 Accurate modelling of left-handed metamaterials using finite-difference time-domain method with spatial averaging at the boundaries *J. Opt. A: Pure Appl. Opt.* **9** 468–75

[18] Zhao Y, Belov P A and Hao Y 2006 Spatially dispersive finite-difference time-domain analysis of subwavelength imaging by the wire medium slabs *Opt. Express* **14** 5154–67

[19] Zhao Y and Hao Y 2007 Finite-difference time-domain study of guided modes in nano-plasmonic waveguides *IEEE Trans. Antennas Propag.* **55** 3070–7

[20] Zhao Y, Argyropoulos C and Hao Y 2008 Full-wave finite-difference time-domain simulation of electromagnetic cloaking structures *Opt. Express* **16** 6717–30

[21] Zhao Y and Hao Y 2009 Full-wave parallel dispersive finite-difference time-domain modeling of three-dimensional electromagnetic cloaking structures *J. Comput. Phys.* **228** 7300–12

[22] Berenger J P 1994 A perfectly matched layer for the absorption of electromagnetic waves *J. Comput. Phys.* **114** 185200

[23] Teixeira F L and Chew W C 1997 PML-FDTD in cylindrical and spherical grids *IEEE Microw. Guid. Wave Lett.* **7** 285–7

[24] Chew W C and Weedon W 1994 A 3D perfectly matched medium from modified Maxwell's equations with stretched coordinates *Microw. Opt. Technol. Lett.* **7** 599–604

[25] Hildebrand F B 1956 *Introduction to Numerical Analysis* (New York: McGraw-Hill)

[26] Brown J 1960 Artificial dielectrics *Prog. Dielectr.* **2** 195–225

[27] Pendry J B, Holden A J, Steward W J and Youngs I 1996 Extremely low frequency plasmons in metallic mesostructures *Phys. Rev. Lett.* **76** 4773–6

[28] Belov P A, Marques R, Maslovski S I, Nefedov I S, Silveirinha M, Simovski C R and Tretyakov S A 2003 Strong spatial dispersion in wire media in the very large wavelength limit *Phys. Rev.* B **67** 113103

[29] Kancleris Z 2008 Handling of singularity in finite-difference time-domain procedure for solving Maxwell's equations in cylindrical coordinate system *IEEE Trans. Antennas Propag.* **56** 610–3

[30] Dib N, Weller T, Scardeletti M and Imparato M 1999 Analysis of cylindrical transmission lines with the finite-difference time-domain method *IEEE Trans. Microw. Theory Tech.* **47** 509–C512

[31] Chen Y, Mittra R and Harms P 1996 Finite difference time domain algorithm for solving Maxwell's equations in rotationally symmetric geometries *IEEE Trans. Microw. Theory Tech.* **44** 832–C838